Article

Sea-ice freeboard and thickness in the Ross Sea from airborne (IceBridge 2013) and satellite (ICESat 2003–2008) observations

Liuxi Tian[1,2] , Hongjie Xie[1,2], Stephen F. Ackley[1,2], Jiakui Tang[1,3], Alberto M. Mestas-Nuñez[1,2] and Xianwei Wang[4]

[1]Department of Geological Sciences, University of Texas at San Antonio, TX 78249, USA; [2]NASA Center for Advanced Measurements in Extreme Environments, University of Texas at San Antonio, TX 78249, USA; [3]College of Resources and Environment, University of Chinese Academy of Sciences, Beijing, China and [4]School of Geography and Planning, Sun Yat-sen University, Guangzhou, China

Abstract

NASA's Operation IceBridge mission flew over the Ross Sea, Antarctica (20 and 27 November 2013) and collected data with Airborne Topographic Mapper (ATM) and Digital Mapping System (DMS). Using the DMS and reflectivity of ATM L1B, leads are detected to define local sea level height. The total freeboard is then obtained and converted to ice thickness. The estimated mean sea-ice thickness values are found to be in the 0.48–0.99 m range. Along the N-S track, sea ice was thinner southward rather than northward of the fluxgate, resulting in two peaks of modal thickness: 0.35 m (south) and 0.7 m (north). This supports that new ice produced in coastal polynyas is transported northward by katabatic winds off the ice-shelf. The lowest (2%) elevation method used for freeboard retrieval for ICESat is also tested for ATM data. It is found that the lowest elevation method tends to overestimate freeboard, but mean values are less affected than mode values. Using mean thickness values of ICESat and ATM along the 'fluxgate', separating the shelf from the deep ocean, the exported ice volume at this 'fluxgate' is found to be higher during the ICESat years (2003–2008) than during the IceBridge year (2013).

1. Introduction

Sea ice plays an important role in heat exchange between the ocean and atmosphere due to its impact and feedback on the transfer of heat, moisture and momentum across the ocean–atmosphere interface (Rinke and others, 2006; Dieckmann and Hellmer, 2010). Polar regions also show high sensitivity to climate change due to the high reflectivity of ice compared to ocean water. This ice-albedo feedback mechanism is a factor that contributes to high polar sensitivity to warming (Holland and others, 2001; Screen and Simmonds, 2010). The sea ice of the two polar regions has experienced different patterns of change since the late 1970s (Turner and Overland, 2009; Simmonds, 2015). In the Arctic, there has been a remarkable reduction of sea-ice extent and thickness (Kwok and Rothrock, 2009; Simmonds, 2015; Meier, 2017). By contrast, based on passive microwave satellite data, a slight increase in Antarctic sea-ice extent has been observed since the late 1970s (Zhang, 2007; Parkinson and Cavalieri, 2012) until a sharp decline occurred in late 2016 (Stuecker and others, 2017; Turner and others, 2017; Kusahara and others, 2018) leading the satellite era minimums observed in 2017 and 2018 (Parkinson, 2019). Much of the previous extent increase had occurred in the region of the Ross Sea (Parkinson and Cavalieri, 2012; Parkinson, 2019). Satellite observations also showed an increase in Ross Sea ice duration. Earlier sea-ice advance and later retreat make the summer ice-free season shorter by 2 months (Stammerjohn and others, 2012). It is still unclear, however, if sea-ice thickness, volume and sea-ice production (SIP) have similarly increased in the Ross Sea.

Coastal polynyas are areas of high SIP, where sea ice is continually blown offshore and replaced by newly formed frazil ice and pancake ice (Gordon and Comiso, 1988). In the Ross Sea, there are three persistent polynyas, including the Ross Ice Shelf polynya (RSP), Terra Nova Bay polynya (TNB) and McMurdo Sound polynya (MCM) (Fig. 1). Those polynyas are a response to both large-scale atmospheric winds and katabatic winds that form over the inland glacier (Martin and others, 2007). As the ice forms within the polynya, the brine it rejects raises the salinity of the water overlying the continental shelf (Gordon and Comiso, 1988). The SIP in those polynyas leads to the formation of the High Salinity Shelf Water (HSSW), which contributes to Antarctic Bottom Water (AABW) formation, thus affecting global thermohaline circulation (Gordon and Comiso, 1988) and ultimately leading to heat and material exchanges between the atmosphere and the deep ocean. In contrast, changes in SIP that occur off the shelf only affect the upper ocean locally and not the deep ocean. The Ross Sea fluxgate (Fig. 1), separating the shelf from the deep ocean, lies over the 1000 m depth contours (Kwok, 2005). Calculation of the exported ice volume depends on the ice thickness. Knowing the thickness distribution is thus critical for estimating the volume export and enables researchers to have a better understanding of the observed freshening in the Ross Sea (Jacobs and Giulivi, 2010).
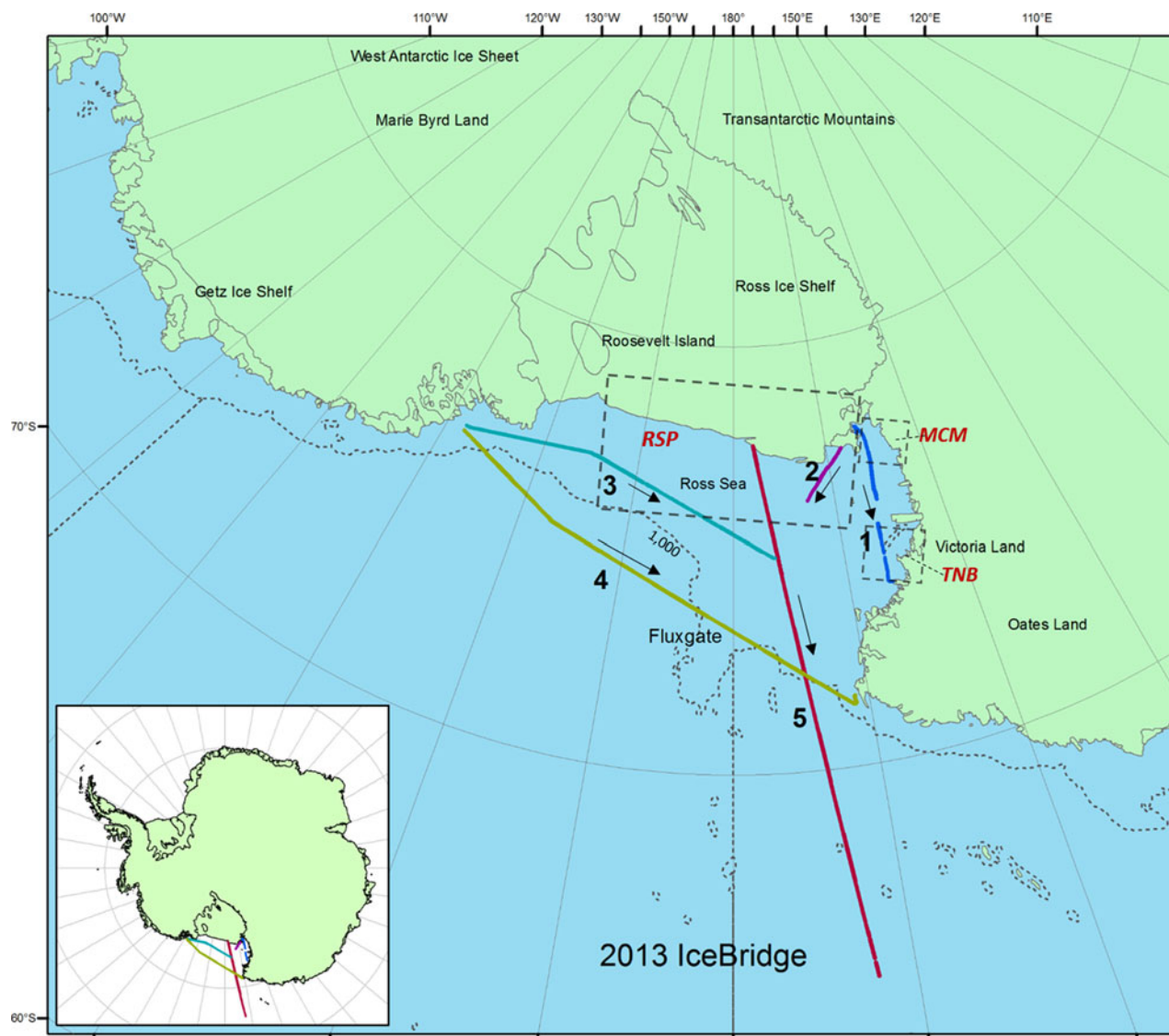
Fig. 1. IceBridge flights (#III and #VI) in the Ross Sea, Antarctica on 20 and 27 November 2013, respectively, with tracks 1, 2, 3, 4 for flight #III and track 5 for flight #VI. Track 4 is the line identified as the Ross Sea fluxgate roughly over the 1000 m bathymetry contour separating the continental shelf to the south from the deep ocean to the north. The arrows show the direction of each track that is used for data analysis and discussion purposes only. The three polynyas are Ross Ice Shelf polynya (RSP), Terra Nova Bay polynya (TNB) and McMurdo Sound polynya (MCM).

The objectives of this study are to (1) compute total freeboard and ice thickness using the data collected from 2013 NASA Operation IceBridge (OIB) airborne overflights in the Ross Sea, (2) examine the distribution of freeboard and ice thickness over the Ross Sea, and (3) compare our results of OIB (2013) with an ICESat freeboard product (2003–2008).

2. Data and methods

2.1 OIB datasets

NASA's OIB mission flew over the Ross Sea, Antarctica (20 and 27 November 2013) and collected important surface sea-ice data with Airborne Topographic Mapper (ATM) and Digital Mapping System (DMS) instrumentation for the first time.

ATM data are the surface elevation data acquired through an airborne Light Detection and Ranging (LIDAR) system using a scanning laser beam (Krabill, 2013). The ATM is a 532 nm wavelength conically scanning laser altimeter with a pulse repetition frequency of 5 kHz and an off-nadir scan angle of ~15° (T2 scanner) or 23° (T3 scanner), combined with a differential GPS system

for aircraft positioning and an inertial navigation system to measure aircraft orientation. The footprint size of each individual elevation measurement is ~1 m, which is set by the laser beam divergence. The ATM data are referenced to the ITRF-2005 reference frame and projected onto the WGS-84 ellipsoid (Krabill, 2013; Kurtz and others, 2013; Wang and others, 2013). Two types of ATM data sets with different resolution are analyzed in this study, ATM L1B (~1 m) and L2 (80 m sample width by ~60 m along track). The L1B data are the ATM Level-1B Qfit Elevation and Return Strength data with all biases and offsets including heading, pitch, roll, ATM-GPS offset, scanner angles, range bias removed. Each surface elevation measurement corresponds to one laser pulse. The measurements have not been resampled. Nominal spatial resolution is 1 m (Krabill, 2013). The L2 data are the ATM Level-2 Ice Elevation, Slope and Roughness data sets that are re-sampled and averaged from ATM L1B data. The L2 elevation measurements have been resampled at the distance interval along the flight track of ~60 m, which is controlled by aircraft speed. Each set of along-track records contains a fixed 80 m across-track nadir platelet as well as three or five additional platelets that together span the
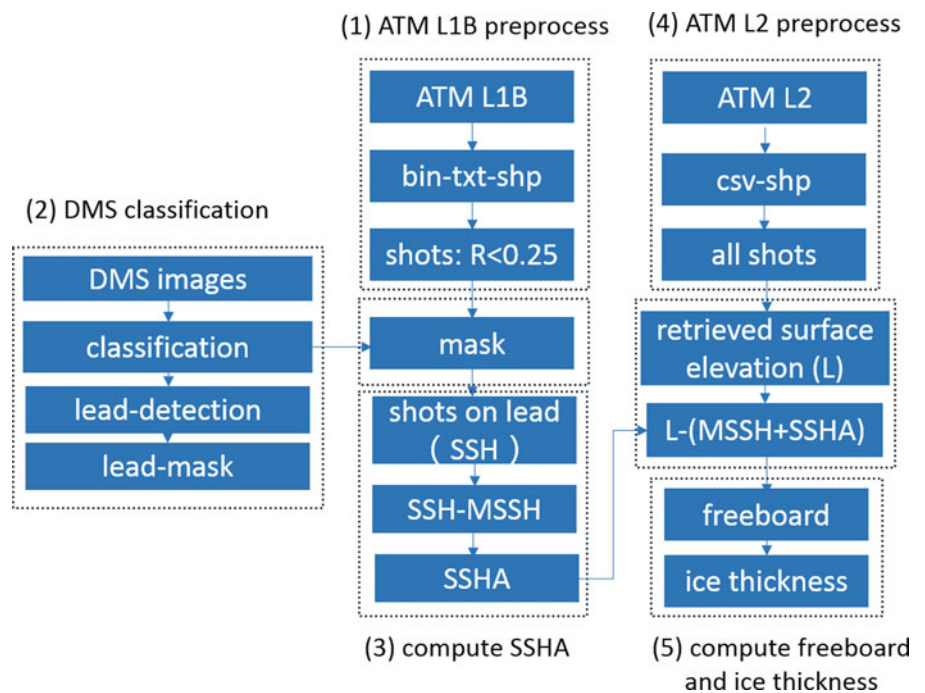
Fig. 2. Workflow chart for deriving total freeboard and ice thickness from IceBridge ATM and DMS data. SSH, sea surface height; MSSH, mean sea surface height; SSHA, sea surface height anomaly.

entire swath of the ATM scan (Wang and others, 2013; Studinger, 2016). L1B data are used to calculate local sea level over leads identified using DMS imagery, while L2 data are used for total freeboard retrieval in this paper.

DMS data, high-resolution natural color and panchromatic imagery, have a pixel resolution from 0.015 to 2.5 m depending on flight altitude (0.1 m at an altitude of 457 m), also is referenced to the WGS84 ellipsoid (Dominguez, 2010).

2.2 ICESat freeboards

In 2003, ICESat was launched by NASA with a Geoscience Laser Altimeter System (GLAS) for measuring surface elevations (Zwally and others, 2002). It sampled the Earth's surface from an orbit with inclination of 94° with footprints of ∼70 m in diameter spaced at ∼170 m intervals (Kwok and others, 2004). The 2003–2008 ICESat freeboard data, which were derived by using a local sea level reference obtained by the lowest (2%) elevation values within a 50 km section (Kern and Spreen, 2015), are used in this study. In order for ICESat data to have enough footprints to do statistics and for comparison with IceBridge data, the full spring seasons (see Table 2 of Li and others, 2018) of ICESat data are used. A buffer zone within a distance of 30 km at each side of each IceBridge track is used to extract the ICESat freeboard values. This allows an approximate colocation of the ICESat and IceBridge data.

2.3 Mean Sea Surface data

The DTU15 Mean Sea Surface Height (MSSH) is used as a geoidal sea level reference to do the geoid correction of ATM L1B and L2. The DTU15 Mean Sea Surface (MSS) released from DTU (Technical University of Denmark) is a global, high-resolution mean sea surface with a resolution of 1 min by 1 min. This is based on the DTU13 model through the usage of multi-mission satellite altimetry gathered from ten different satellites (Andersen and others, 2015). Merging of Cryosat-2 LRM, SAR and SAR interferometry (SAR-In) data and the down-weighting of ICESat data are significant recent advances that provide greater advantages over previous MSS estimates (Andersen and others,

2016; Skourup and others, 2017). The averaging period of this MSS is 1993–2012. The MSS is the sum of geoid and ocean mean dynamic topography (Andersen and others, 2016).

2.4 Lead detection and sea-ice thickness retrieval methods

To calculate total freeboard, an instantaneous local Sea Surface Height (SSH) reference must be determined first (Kurtz and others, 2009; Xie and others, 2013). The key location used to obtain SSH is through the identification of leads (open water or very thin ice) (Xie and others, 2013; Wang and others, 2016). There are four main methods used to obtain SSH. The first is to take a percentage of lowest-elevation points along a range distance of a flight track, and calculate the average height of these points (Zwally and others, 2008). We call this 'the lowest elevation method' in this study. The second and third methods are to identify leads/water either by the apparent reflectivity of the transmitted laser pulse (Kwok and others, 2012) or by the waveform characteristics of radar altimetry data (Farrell and others, 2009). The apparent reflectivity is defined as the ratio of the reflected laser signal strength to the transmitted signal strength (Wang and others, 2016). Leads have low apparent reflectivity. The raw data of radar altimetry satellite are recorded as a waveform (power in y-axis and gate number in x-axis) (Nababan and others, 2018). Echo waveforms from lead footprints have one single peak with high echo power (Xia and Xie, 2018). These three methods, used with satellite altimetry data, have limitations due to the paucity of optical images to verify results. The fourth method, only available from airborne data, is to use optical images that are collected simultaneously with the laser altimetry data to visually identify leads and their average height of the laser shots within leads is then taken as the lead surface height (Kurtz and others, 2013; Onana and others, 2013; Wang and others, 2013; Wang and others, 2016). Since the reflectivity of laser shots on thick sea ice is much higher than on leads (Kwok and others, 2012), reflectivity values can be used to exclude misclassified leads (Wang and others, 2016).

In this study, we combine the DMS-mapped leads and L1B laser shots on leads to get the most realistic local sea levels, then apply to L2 data for freeboard retrieval, as our objective
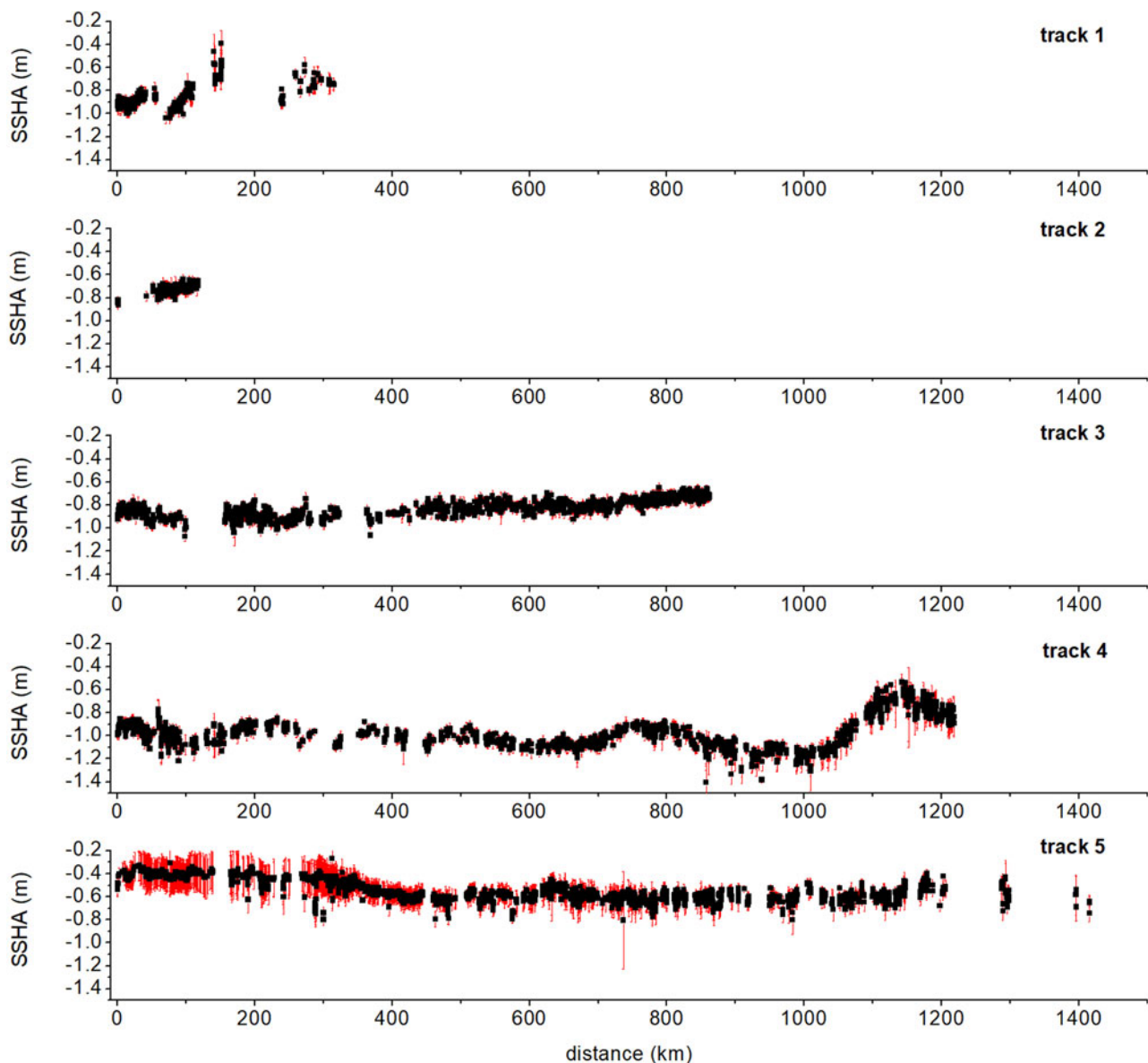
Fig. 3. Local sea surface height anomaly (SSHA, black) with ±1 std dev. (red), along the distance direction (start and end) as indicated in Figure 1.

method. We also apply the lowest (2%) elevation method to provide a reference for later evaluation, in order to compare with satellite altimetry from ICESat. We compare the total freeboard derived from these two methods to evaluate how each method affects the results.

Total freeboard can be converted to ice thickness through different approaches: buoyancy equation method (Zwally and others, 2008; Weissling and others, 2011), zero sea-ice freeboard assumption method (Kurtz and Markus, 2012) and empirical equation method (Xie and others, 2011; Ozsoy-Cicek and others, 2013; Li and others, 2018). For the buoyancy equation, accurate estimates of snow depth and densities of snow, sea ice and seawater are essential for deriving an accurate estimate of ice thickness (Zwally and others, 2008; Weissling and others, 2011). The major limitation of using a buoyancy equation in Antarctica is the uncertainty of snow depth retrieval (Markus and Cavalieri, 1998). In this 2013 Ross Sea campaign, snow depth data through the snow radar is not available, and therefore, the buoyancy equation is not feasible. From both approaches of zero sea-ice freeboard assumption and empirical equation, however, sea-ice thickness can be directly estimated from total freeboard without knowing snow depth. The zero sea-ice freeboard assumption

approach assumes that snow depth is equal to the total freeboard (Kurtz and Markus, 2012), which is not always true, particularly for thinner ice with no snow cover at all. This could result in an underestimate of sea-ice thickness (Kwok & Kacimi, 2018; Kern and others, 2016). The empirical equation approach provides a direct conversion of total freeboard into sea-ice thickness, totally based on field measurements. For this Ross Sea case, the empirical linear equation between ice thickness and total freeboard was derived from the measurements of 23 profiles (of 50–100 m in length each) during the NB Palmer September/ October 1994 cruise (Jeffries and others, 1998; Ozsoy-Cicek and others, 2013) and is used for this study. Based on their study (Ozsoy-Cicek and others, 2013), the R2 of the empirical equation is 0.83, meaning this linear equation could explain 83% of the measured ice thickness variation.

2.5 Objective method

A flow diagram of the objective method using DMS and L1B with the laser shots reflectivity to identify leads is shown in Figure 2 and a description of each step is given below.
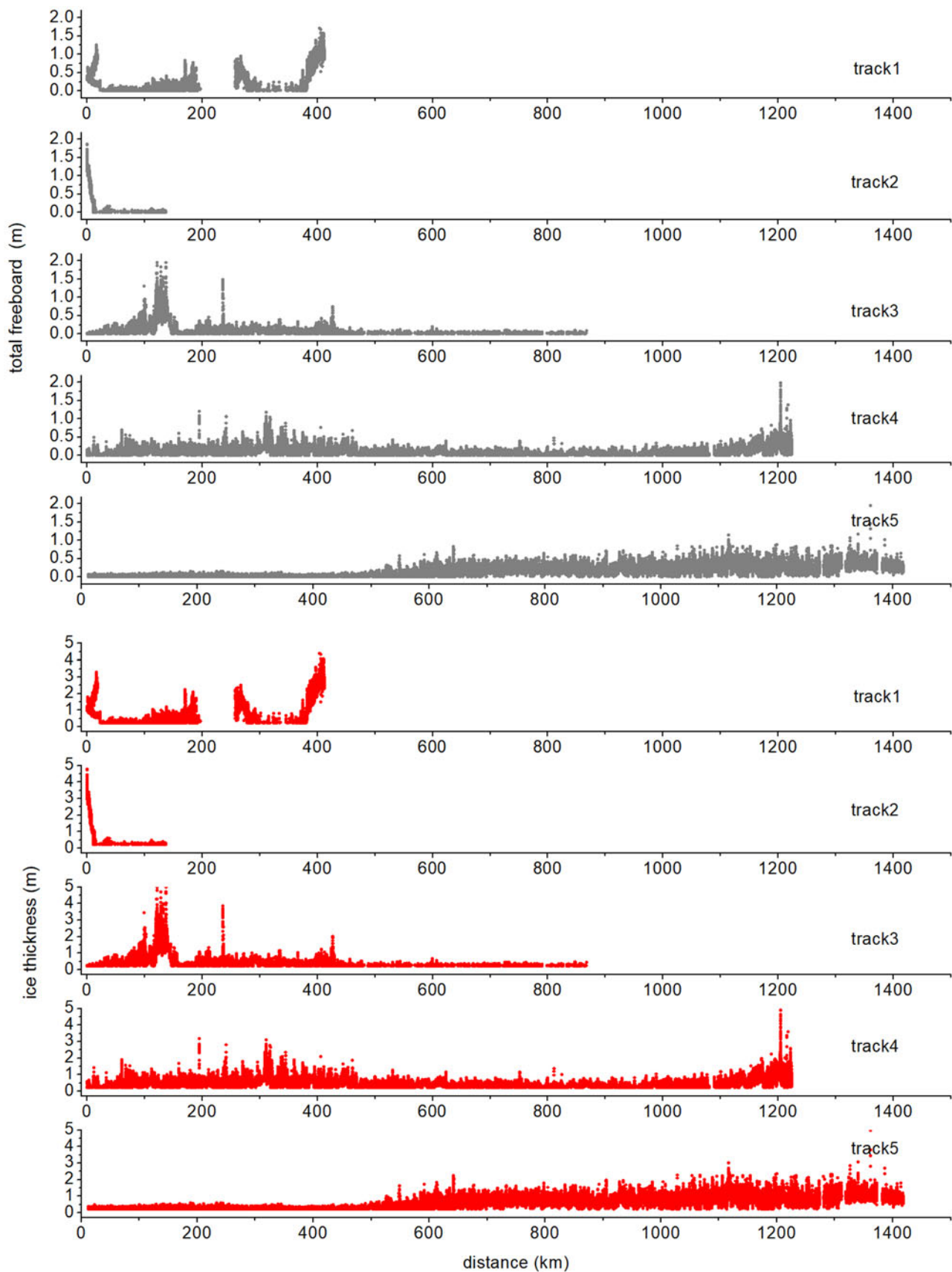
Fig. 4. Total freeboard (top panels, gray) and derived ice thickness (bottom panels, red) as a function of distance along each track.

2.5.1 DMS classification

Leads are optically dark features with low reflected pixel intensities (DN values) while snow/sea ice have high reflected pixel intensities in high-resolution natural color DMS photographs.

The distribution of pixel intensities thus provides a practical way to separate leads from sea ice (Onana and others, 2013; Wang and others, 2016). Wang and others (2016) found that the pixel intensities of leads and snow/thick sea-ice surface had
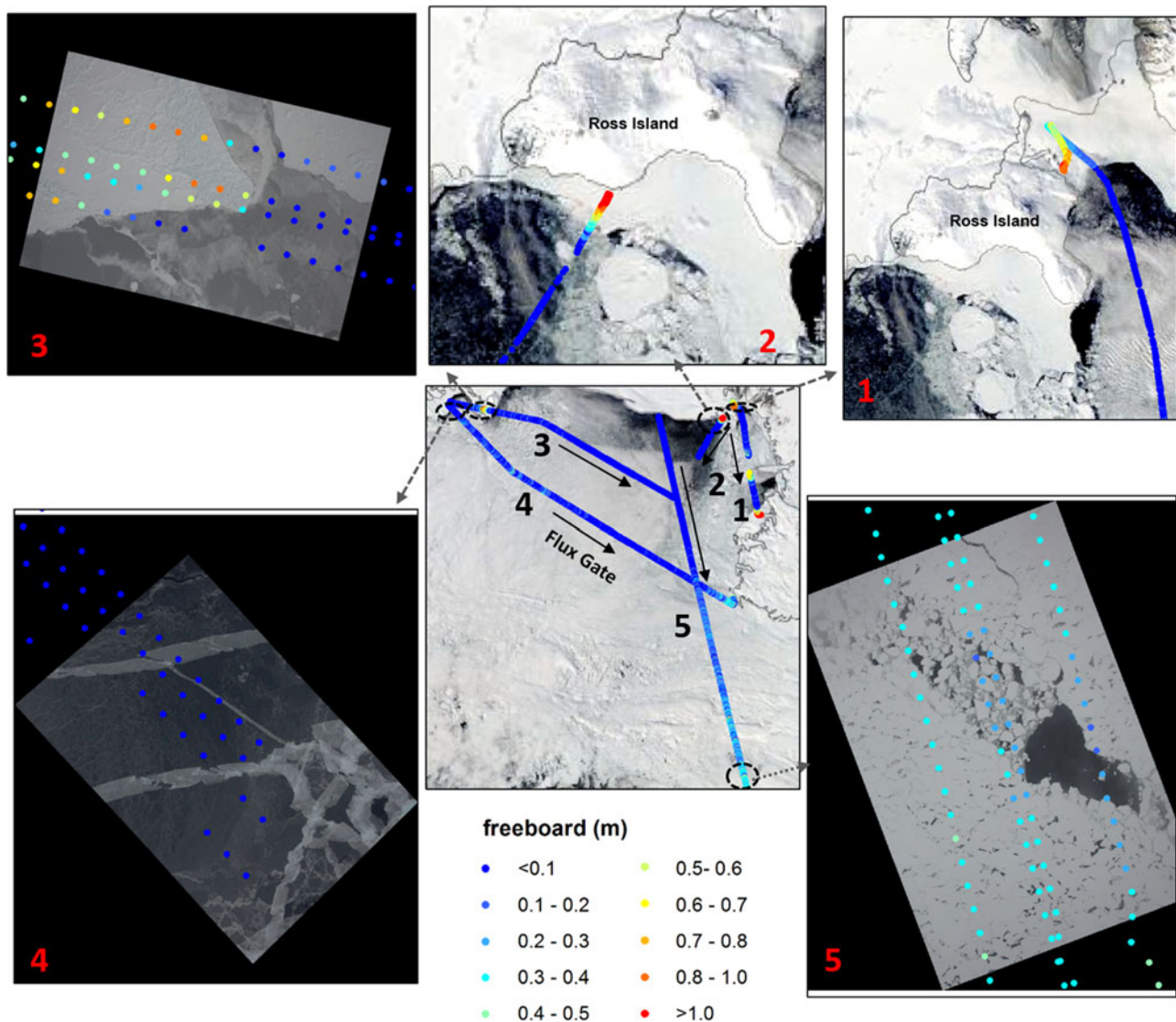
Fig. 5. Spatial distribution of freeboard along each track (center) with a zoom-in window showing the ATM L2 shots on DMS imagery (track 3, 4 and 5) and MODIS imagery (tracks 1 and 2) for sampled ice types on different tracks. Tracks 1 and 2 had an apparent abrupt increasing freeboard (ice thickness) toward the Ross Island (see the zoom-in windows 1 and 2) with freeboard exceeding 1 m. The MODIS true color image was on 20 November 2013, the same day as the tracks 1 and 2.

two distinguishable modes and can be used to develop dynamic pixel intensity thresholds to do the classification. As the pixel intensities of snow/sea ice are determined by the solar illumination and vary with the Sun elevation and weather conditions, dynamic thresholds varying from image to image, instead of a fixed threshold for all images, are used in this study to detect the leads. We use this principle to manually select all the images with the leads first and then automatically detect the first mode value (mode of leads) image by image to do the classification. The lead class is then transformed into a shapefile and used as a mask (Fig. 2).

2.5.2 ATM L1b and ATM L2 preprocessing
Both ATM L1B and L2 data are processed into shapefile data. Because the reflectivity of laser shots on thick sea ice is much higher than on leads, the reflectivity value (R) of 0.25 (Kwok and others, 2012) is set as the threshold of L1B data to extract lead shots, i.e., $R < 0.25$ as leads. Misclassified leads are then excluded by using the DMS-derived lead mask. By combining DMS images (leads mask) and the reflectivity of ATM L1B, sea surface shots within leads are determined. Shots of both L1B and L2 are then processed with geoid correction by subtracting

DTU 15 MSSH (Fig. 2). We then use ATM L2 to calculate total freeboard. In this study, we use Sea Surface Height Anomaly (SSHA) instead of SSH.

2.5.3 Computation of SSHA
After sea surface shots of one lead are detected, the elevation average after geoid correction (i.e., SSH-MSSH) is computed as SSHA of this lead. Shots falling outside one std dev. are treated as outliers and deleted. Weighted inverse distance interpolation is used to predict the SSHA at locations without leads present. The SSHA profile along each flight track is then obtained.

2.5.4 Computation of freeboard and ice thickness
Total freeboard (F) is calculated by using the surface elevation of ATM L2 minus the corresponding DTU 15 MSSH and SSHA. Ice thickness is then retrieved from total freeboard by an empirical equation (Ozsoy-Cicek and others, 2013), derived from ice thickness and freeboard surveys in the Ross Sea region:
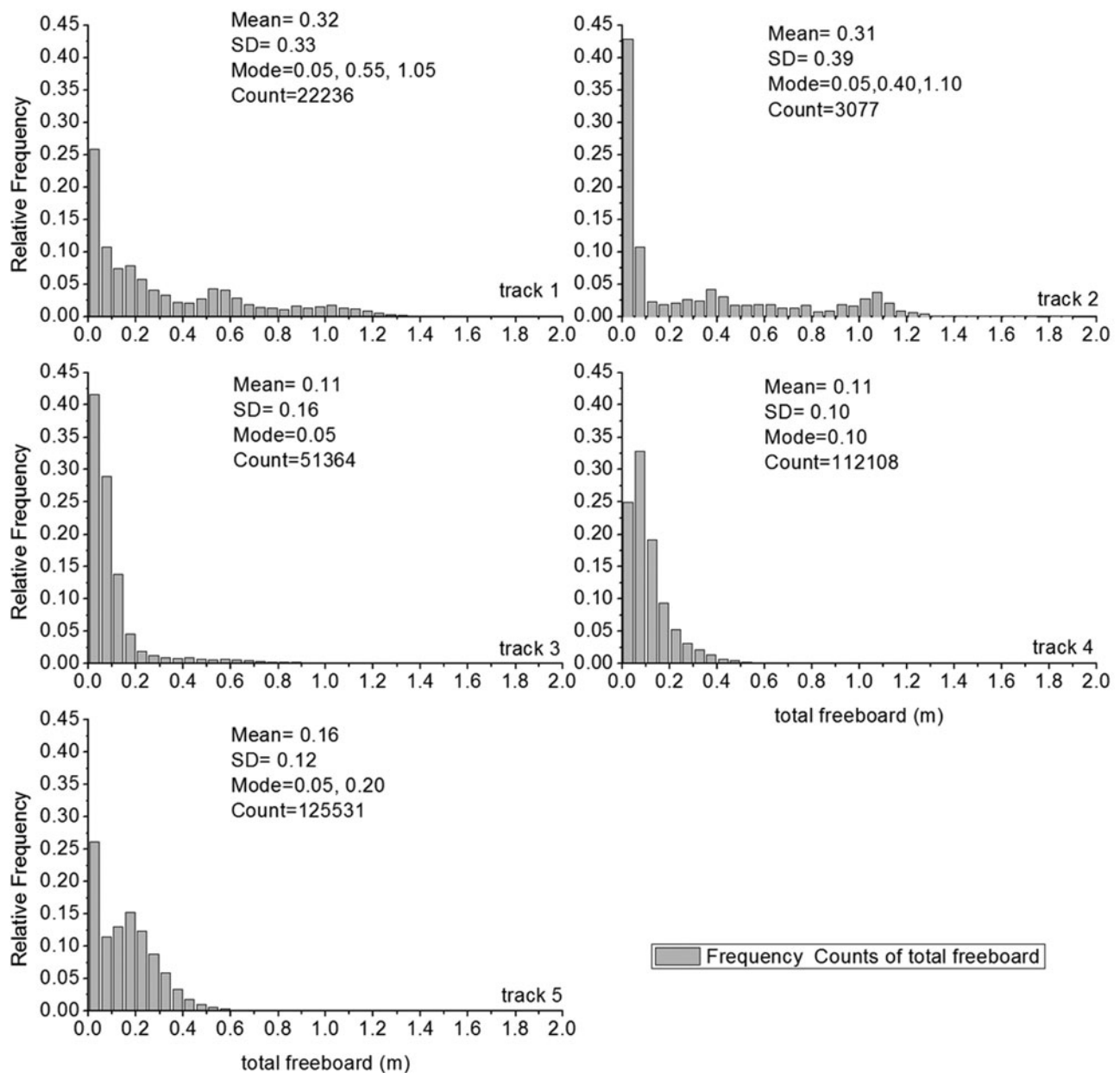
$$I(m) = 2.45 \times F + 0.21. \tag{1}$$

Fig. 6. Frequency distributions of freeboard (top panels, gray) and ice thickness (bottom panels, red) with mean, std dev. (SD), mode and total count number for each track.

2.6 The lowest elevation method

When optical images are not available concurrently with satellite altimetry, previous researchers have used a percentage of the lowest-elevation points along a flight track range, and then calculated the average height of these points as the local sea level (Zwally and others, 2008). When using the lowest elevation method, another key factor is the length of the section that is chosen to determine the local sea level. Since previous studies used both 25 and 50 km sections in processing ICESat data (Zwally and others, 2008; Kern and Spreen, 2015), these two section lengths have thus been used in this study for comparison.

3. Results

3.1 Sea Surface Height Anomaly

Figure 3 shows lead SSHA for all tracks. Track 5 has the highest SSHA with the largest std dev. The std dev. quantifies how close the shot SSHA values are to the mean value. Once the

shot SSHA value exceeds one std dev. away from the mean value, we treat it as an outlier. These outliers can be either indicative of thicker ice or reflection beneath the water surface and are not representative of the true sea level.

3.2 Distribution of freeboard and ice thickness in the Ross Sea

The total freeboard and ice thickness distributions along the five Ross Sea tracks are shown in Figures 4 and 5. Both tracks 1 and 2 show evidence of very thick ice, likely caused by thick ice proximity to the coastal area.

Along tracks 3 and 4 (Figs 4 and 5), thick ice is evidenced along the east section of track 3 and the east and the far west sections of track 4. These thickened ice locations could be attributed to older ice on the east and ridged ice elsewhere. The majority of the ice, however, is thin ice with a modal value of 0.35 m for track 3 and 0.45 m for track 4 (Fig. 6), thinner southwards and thicker northwards. Track 4 was designed to follow the fluxgate (Fig. 5), separating the continental shelf region to the south from the deep
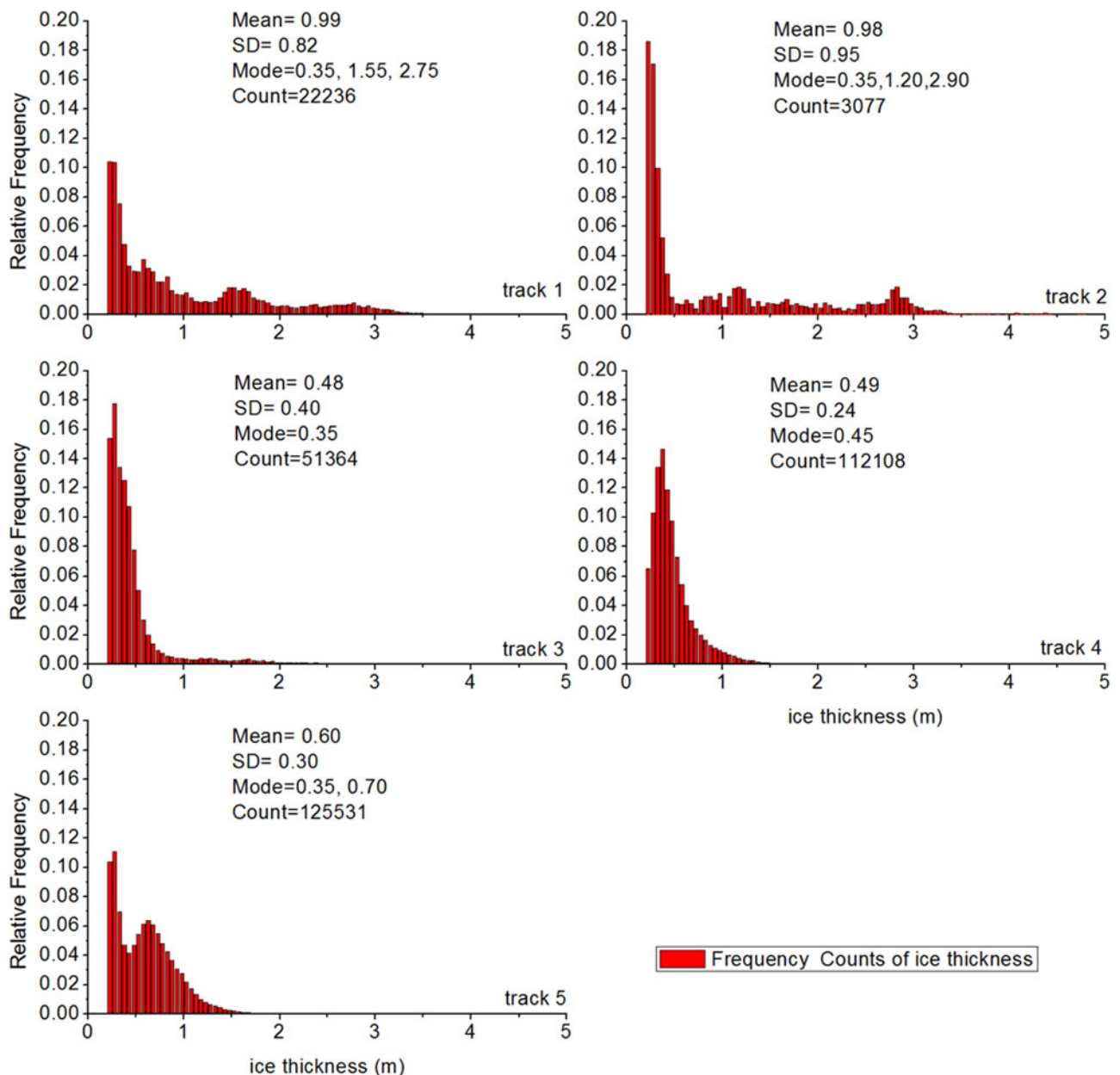
Fig. 6. Continued.

ocean to the north, where ice produced from the coastal polynyas is exported. It is clear that the ice is relatively thinner in the middle section of the fluxgate in comparison to the west and east sections (Fig. 4). This is evidence of ice produced in coastal polynyas (RSP, TNB and McMurdo Sounds polynya) which is pushed northwards due to katabatic winds off the continent (Parish, 1988) with the ice becoming thicker as it grows with age as it moves away from the polynyas. This phenomenon is best supported by the thickness distribution along track 5, starting from the RSP and ending north 1400 km away, with two peaks of modal thickness: 0.35 m to the south and 0.7 m to the north (Figs 4–6).

The histograms of freeboard and thickness along tracks 1 and 2 (Fig. 6) include three modes for freeboard: 0.05, 0.55 and 1.05 m (track1) and 0.05, 0.40 and 1.10 m (track 2); and for ice thickness: 0.35, 1.55 and 2.75 m (track 1) and 0.35, 1.20 and 2.90 m (track 2). The first mode represents the new and young ice in the region and it is the dominant ice type. This is mostly produced in the polynyas due to the katabatic winds continuously pushing new ice away and ice forming in the open water behind it. As the ice drifts

northwards, it thickens thermodynamically with age. The third mode indicates the thickest and ridged ice, although amounting to only a small portion of the ice along the two tracks. For example, the thickest ice of tracks 1 (up to 3 m) and 2 (up to 5 m) is very close to the Ross Island where thick fast ice develop (Fig. 5).

3.3 Comparison of OIB total freeboard from different methods

Figures 7 and 8 show that the results from this method which detects leads by combining DMS images and reflectivity of ATM L1B and the method used the lowest 2% elevation at 25 or 50 km range (Figs 7 and 8). The track 5 from this study has two clear modes rather than one single mode from the lowest elevation method (Fig. 7). Interestingly, the mean values estimated from both methods are nearly the same (Fig. 8). This comparison indicates that lowest elevation method may overestimate the freeboard and not be able to differentiate the thin ice types from in the distribution of freeboards (>6 cm), but mean values of the distribution are affected less (<9 cm).
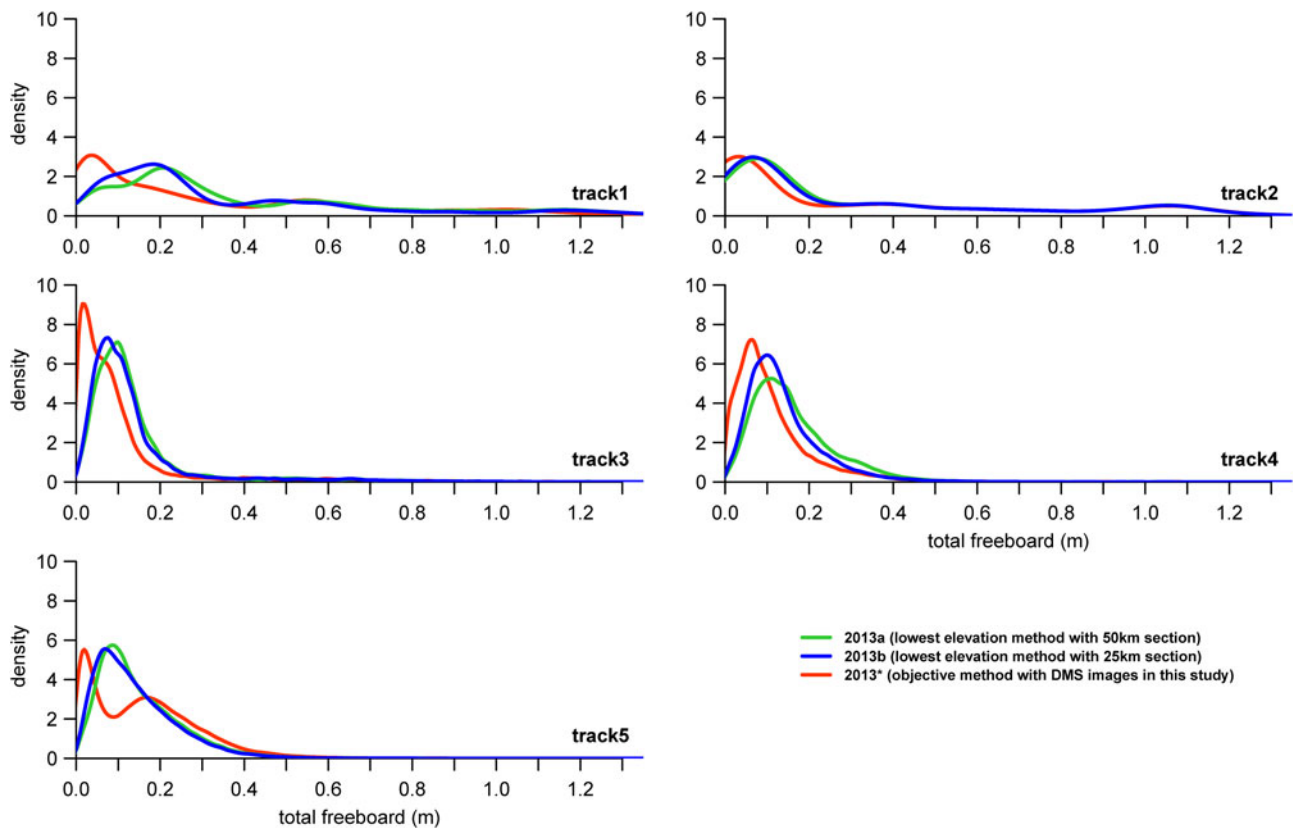
Fig. 7. Kernel density distributions of freeboard (from IceBridge 2013 Ross Sea data) with different methods: using DMS images and ATM derived local sea level (red, objective method in this study), the lowest 2% elevations of 25 km along track as local sea level (blue), and the lowest 2% elevations of 50 km along track as local sea level (green). Kernel density estimation (KDE) is a widely used non-parametric way to estimate the probability density function of a random variable, and it is a smoothing technique to visualize the discrete histogram (Duong, 2007).

Although similar patterns in the distributions (Figs 7 and 8), the 25 km section method results in lower freeboards than the 50 km section method and it is closer to the freeboard mean values (within 5 cm) derived from our objective method.

3.4 Comparison of OIB (2013 a) with ICESat (2003–2008)

The 2003–2008 ICESat freeboard used in this paper was derived from the lowest 2% elevation of 50 km section method (Kern and Spreen, 2015) and can be compared with the 2013 OIB freeboard from the lowest (2%) elevation method with 50 km section (2013 a) to examine the interannual differences. Mixed results are found, with no clear trend from the ICESat 2003–2008 era to 2013 (Fig. 9). In terms of mean ice thickness (Fig. 10), there is a clear increase along the two short tracks (1 and 2) but no change or slight decrease for ice along the other three long tracks. Track 5 is the most stable track, and does not have much change from 2003 to 2013 (Figs 9 and 10). In general, the ice thickness in 2006 and 2007 was thicker (Figs 9, 10 and 12).

4. Discussion

Although the mean reflectivity values of leads for all 2013 IceBridge tracks in the Ross Sea are <0.25, it is found that the reflectivity could change with a few gaps even in one track (Fig. 11). For tracks 2 and 5, most reflectance values are 0.15 or below, indicating it could overestimate the amount of leads if a single threshold value of 0.25 is used for separating leads from thick ice as done in Kwok and others (2012). The major reason for such variances may be due to weather conditions and the difference in solar elevation angles along tracks, though the surface reflectance itself does not change, unless the surface changes. Therefore, to get an accurate separation of leads from thick ice, a section by section or time by time determination of the lead reflectance is required.

Wang and others (2016) found that, within a 45 km section of one ATM L1B track, the SSH demonstrates a linear gradient, which is applied to derive SSHs where there are no leads. In this study, a similar linear gradient of the SSHA was found within a 45 km section, but with several fluctuations along the whole track (Fig. 3). So, considering the entire long track, the Inverse Distance Weighting method is a better method to interpolate the SSHA for the locations without leads, by using a linear combination of values at sampled points weighted by an inverse function of the distance from the point of interest to the sampled points (Li and Heap, 2008).

In this paper, we use the empirical equation to calculate sea-ice thickness. The equation was derived from in situ measurements on Ross Sea taken by Palmer September and October 1994 cruise (Ozsoy-Cicek and others, 2013). Kern and others (2016) intercompared different methods to retrieve sea-ice thickness, including empirical equation, equation with zero sea-ice freeboard assumption (Kurtz and Markus, 2012) and the physically-based method with snow depth as an input. They found common to all approaches is the thin sea-ice thickness of 1–2 m in the Ross Sea downstream of the RSP (Figs 2, 5, Kern and others, 2016). Further, values derived from empirical equations are higher than those from the zero sea-ice freeboard assumption approach but lower than those from the physically-based method. The sea-ice thickness around the fluxgate could be 1 m lower than the physically-based method (Fig. 5, Kern and others, 2016). Considering the complexity of snow depth in the Ross Sea and
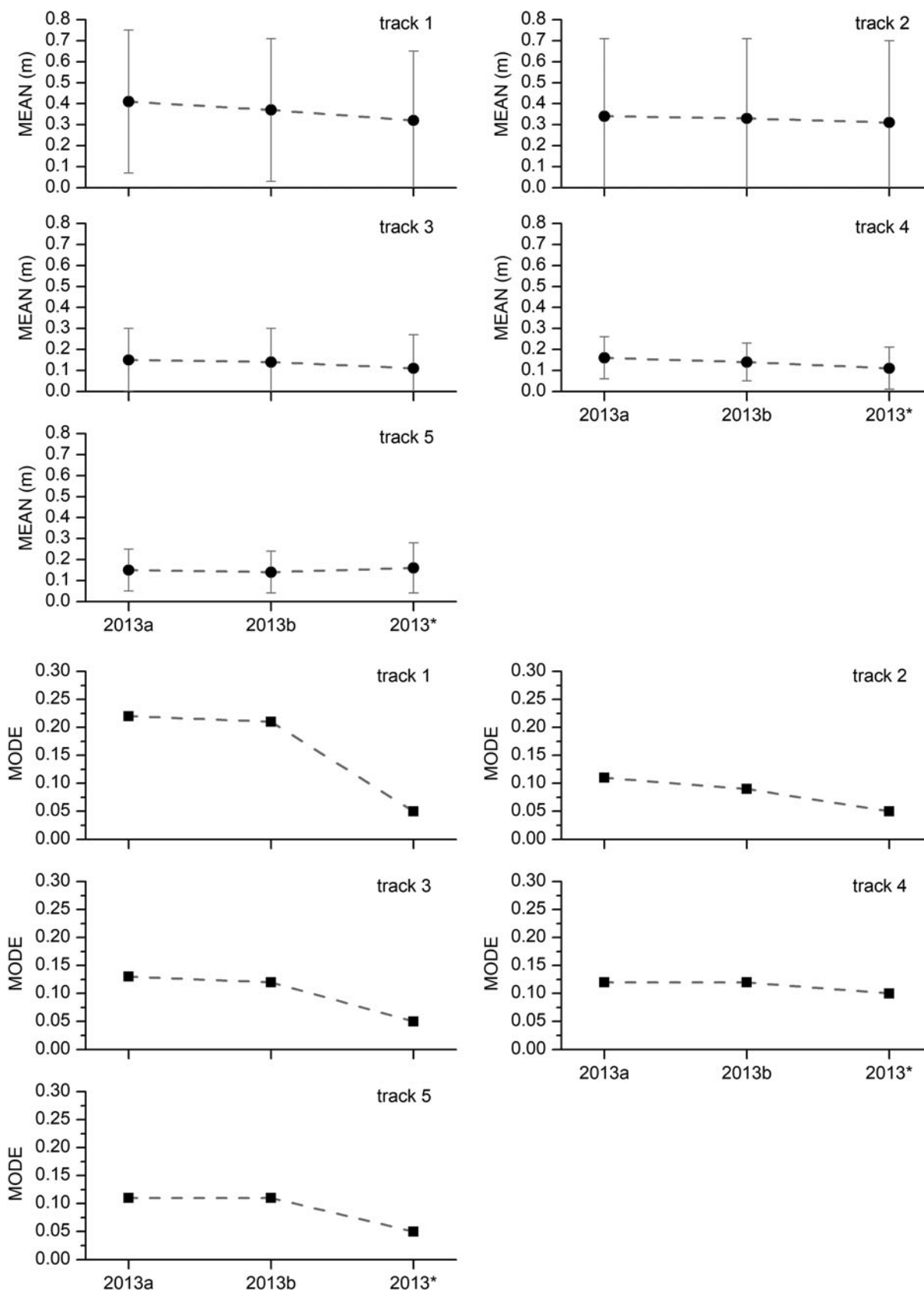
Fig. 8. Mean (m) and principal (most frequent) modal value (m) of freeboard (from IceBridge 2013 Ross Sea data), with a, b and *, respectively, referring to the 50 km, 25 km lowest (2%) elevation methods, and the objective method combined with ATM and DMS as described in Figure 7.

the limitation of field measurements, a thorough analysis of uncertainties is hard to make. The scientific cooperation and data sharing could provide effective ways to develop the methods of thickness retrieval in the near future.

The objective method combining the use of the DMS and L1B can provide a more accurate local sea level for deriving total free-board in comparison to the lowest elevation method which only uses elevation data. The results of this study provide a reference
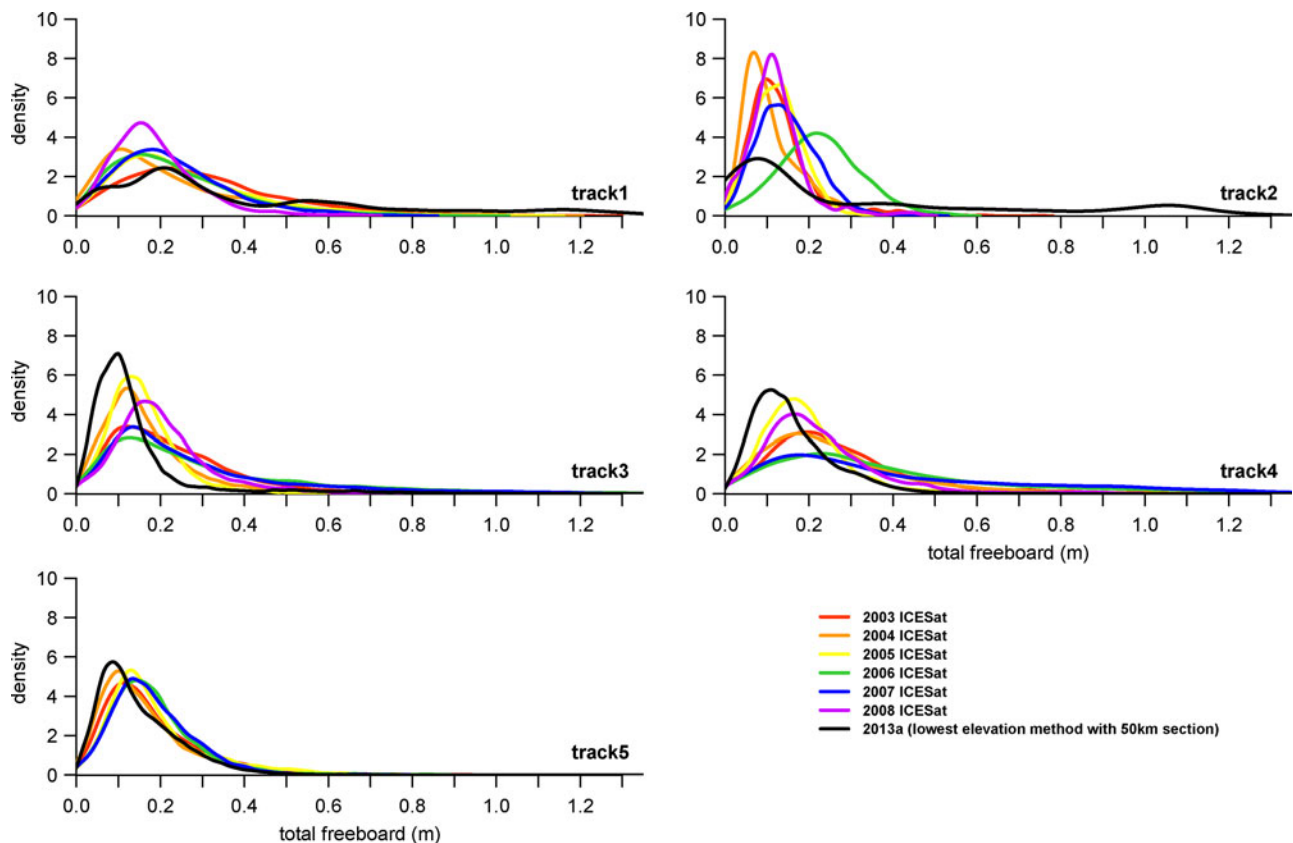
Fig. 9. Kernel density distributions of freeboard (from IceBridge 2013 Ross Sea data) based on the lowest 2% elevations of 50 km along track as local sea level and 2003–2008 ICESat total freeboard using the same method (2% with 50 km).

to evaluate the lowest elevation method. It is found that the lowest elevation method overestimates the freeboard, especially the lowest peak of freeboard distribution. It also indicates that the mean values are less affected than mode values, because spatial aliasing on sea-ice thickness raises the mode value impact but affects the mean less (Geiger and others, 2015). High-resolution optical imagery, however, is not always available, for example, for ICESat and ICESat-2. Using a better method to derive local sea level from ICESat-2 is very important (Markus and others, 2017) and requires further study. The results also show the freeboard from 25 km range method is closer to our results than the 50 km range derived freeboard. This could provide a reference to researchers on determining the optimal distance-section when using the lowest elevation method.

Using the same method when comparing the ICESat freeboard with the 2013 OIB freeboard (2013 a) results is in no clear trend in the time ranging from the ICESat era to 2013, although some year-to-year variability is observed. This comparison has two limitations as different date period and location of the tracks (Fig. 12) are used when this comparison is made. To gather adequate ICESat statistical evidence, the spring seasons (see Table 2 of Li and others, 2018) of ICESat data are included, and a buffer zone within 30 km of each side for each IceBridge track is used to extract the ICESat freeboard values (Fig. 12). We expect that the ICESat-2 provides much more effective footprints due to its six beams, 17 m footprint and the 0.7 m intervals along track.

Figure 12 shows the freeboard spatial distribution of ICESat 2003–2008 and 2013 OIB with three different methods. It indicates a similar distribution pattern, being thinner in the center part (gray circle), and thicker in the east, north or near coastal (but not the polynyas). This supports the hypothesis that ice produced in coastal polynyas (i.e., Ross Ice Shelf, Terra Nova Bay and McMurdo Sound) is pushed away to the north due to katabatic

winds off the continent (Parish, 1988) and the ice thickens as it ages and is deformed further away from the polynyas. It also indicates all these methods can provide a relatively good spatial distribution to a certain degree, though some differences in absolute values.

Calculation of the exported ice volume from the Ross Sea polynyas depends on the ice thickness. Area flux can be converted to volume flux by multiplying the area by ice thickness measurements. Most researchers (Kwok, 2005; Martin and others, 2007; Comiso and others, 2011; Drucker and others, 2011) use an average of the ice thicknesses measured by Jeffries and Adolphs (1997) from shipboard inside the fluxgate in the western Ross Sea during May–June 1995, where they found an average thickness of 0.66 ± 0.33 m. However, this estimate neglects the space/time variability in sea-ice thickness as well as the thicker multi-year ice fraction. Year to year variations in mean thickness would change the total volume exported, independent of the net areal export. Track 4 was designed to follow the fluxgate through which newly produced ice from the coastal polynyas is exported. Table 1 shows a comparison of mean sea-ice thickness values along the fluxgate by this research and shipboard. It indicates that mean ice thickness estimates experienced great change from 1995 to 2013. Comiso and others (2011) estimated that the positive rate of increase in the net ice area export is $\sim$30 000 km^2 a^{-1} over the Ross Sea Shelf from 1992 to 2008 and the corresponding volume transport is $\sim$20 km^3 a^{-1} (similar to Drucker and others, 2011) using a 1995 shipboard mean ice thickness of 0.6 m. ICESat data provided a mean sea-ice thickness of 0.93 m from 2003 to 2008 (Table 1), which indicated a much larger volume transport over 2003–2008 than 2013 ATM with optical images that show a mean thickness of only 0.48 m (Table 1), which gives a more precise value for recent year's volume transport estimation. Kwok and others (2017) examined
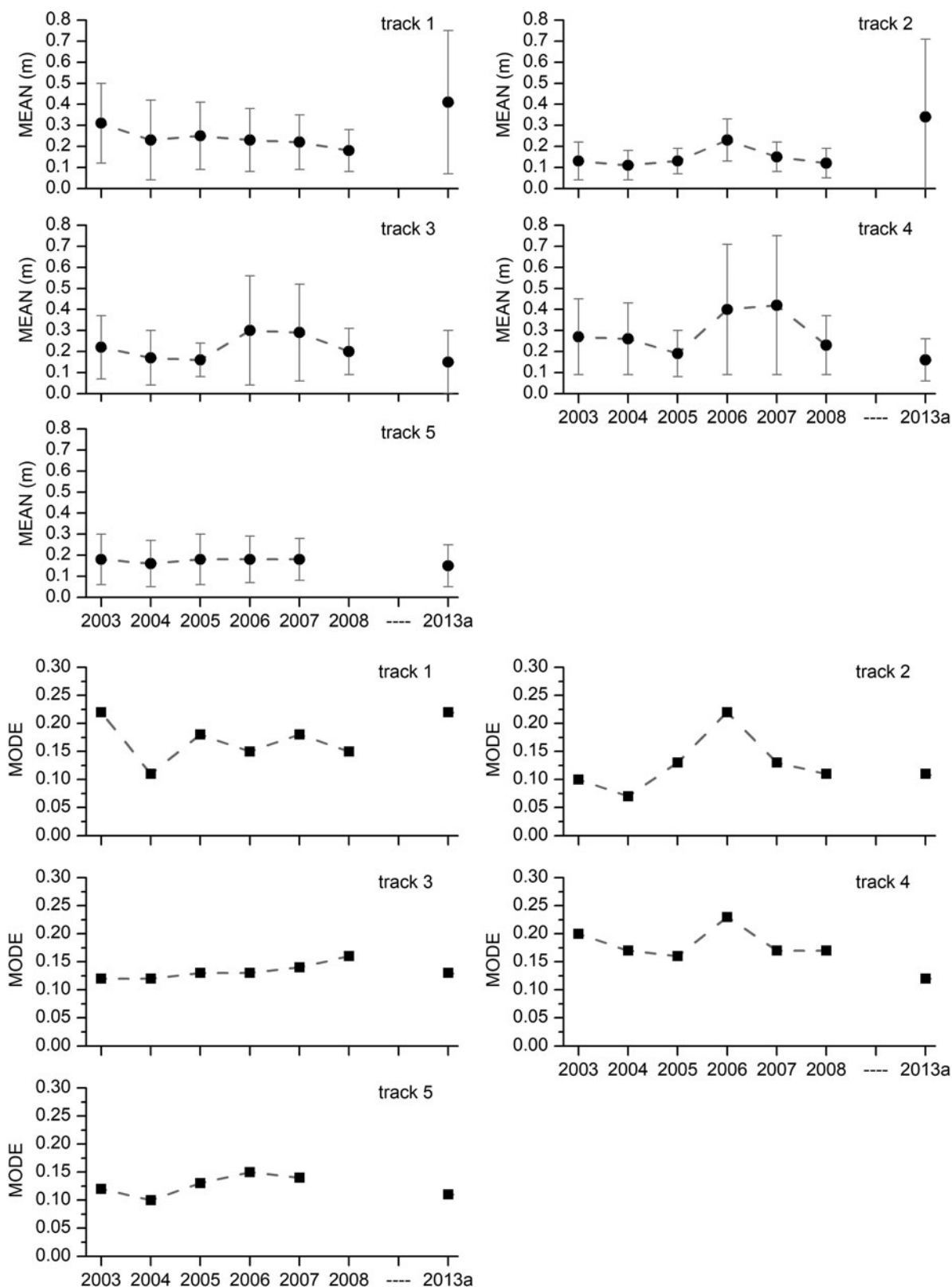
Fig. 10. Mean (m) and modal value (m) of total freeboard from ICESat (2003–2008) and ATM (2013 a, here 'a' refers to 50 km lowest 2% elevation as described in Fig. 7).

mean exportable sea ice at the fluxgate as 750×10^3 km^2 in the past 33 years, with an increase of 7.7×10^3 km^2 a^{-1} from 1982 to 2015. These thickness values could then help to give an estimation of exported ice volume at the fluxgate (Table 1). Using mean thickness values along track 4 from both ICESat and ATM exported ice volume at the flux gates is estimated as higher for the ICESat years (2003–2008) than for the IceBridge year

(2013) (Table 1). Track 5 starts from the RSP and ends north 1400 km away, the ice thickness is clearly thinner than that northwards from the fluxgate with a clear two peaks of modal thickness: 0.35 m to the south and 0.7 m to the north (Figs 4–6). This can provide a correct estimate of the ice volume over the continental shelf. Knowing thickness distribution is critical for estimating the volume export and will help researchers to better specify SIP in
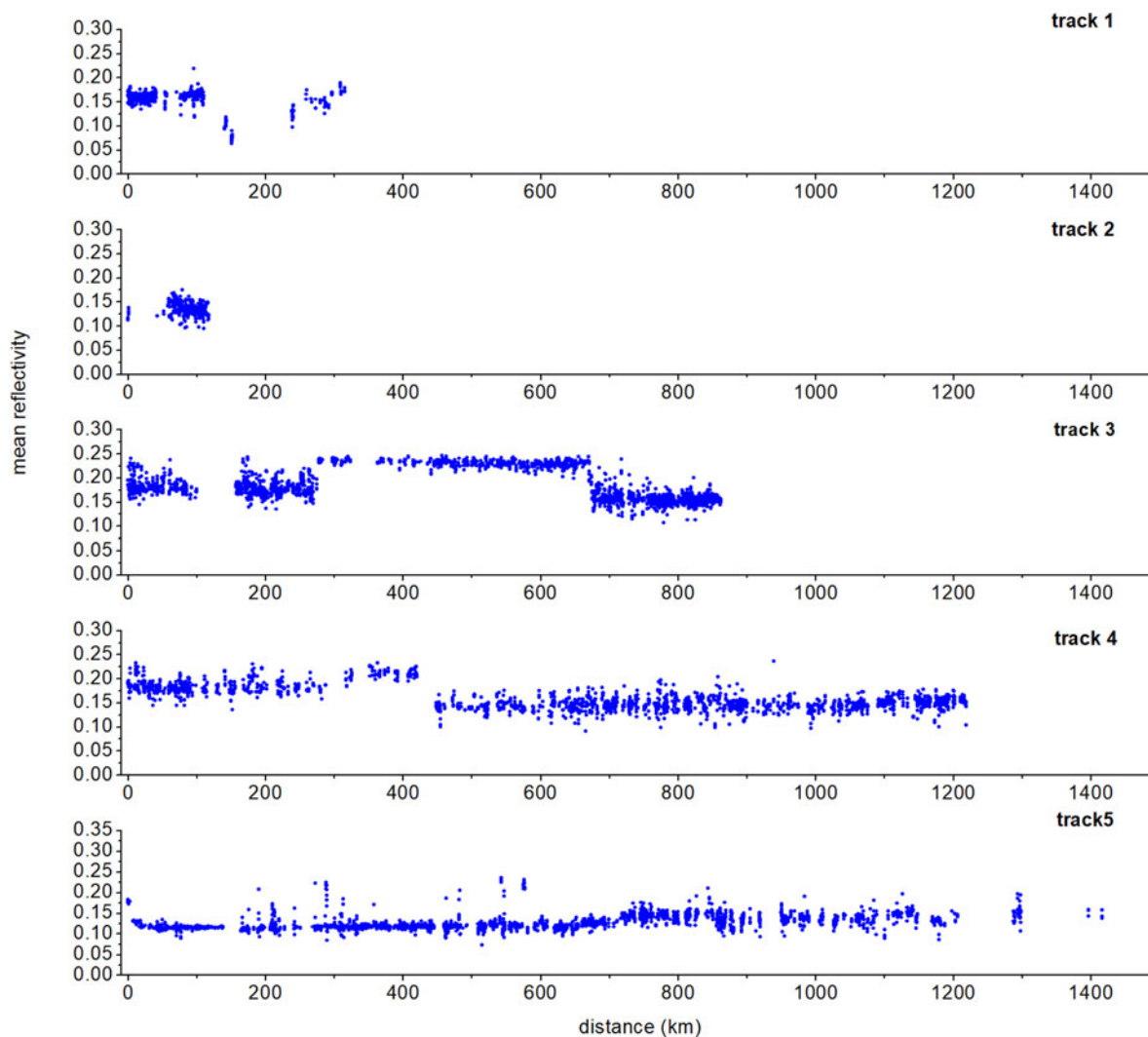
Fig. 11. Mean reflectance (blue) of all L1B shots within leads along the five tracks, with the distance direction (start and end) as indicated in Figure 1.

the Ross Sea. The implications for the formation of dense shelf water and its recent changes by SIP can then be calculated more accurately, developing a better understanding of the observed freshening in the Ross Sea (Jacobs and Giulivi, 2010). Differentiating the ice thickness north and south of the fluxgate is important for obtaining an accurate estimate of the ice volume over the continental shelf.

5. Conclusions

In this study, leads are detected by combining DMS images and reflectivity of ATM L1B, and local sea level are retrieved from ATM L1B shots over leads. Freeboard estimates are obtained from the difference between surface elevation of ATM L2 and the local sea level. Finally, total freeboard is converted to ice thickness through an empirical equation, which does not require knowledge of the snow depth. The OIB 2013 data in the Ross Sea are examined. The results show the dominant ice thickness modal values of all tracks are between 0.35 and 0.45 m, with mean ice thickness values between 0.48 and 0.99 m. The sea-ice thickness along track 5, starting in the RSP and ending 1400 km to the north, is clearly thinner to the south than to the north of the flux-gate with two well-defined modal thickness peaks: 0.35 m to the south and 0.7 m to the north. This is evidence that the ice produced in coastal polynyas when transported from the shelf northwards by katabatic winds becomes thicker as it grows in age and deformation

away from the polynyas. This phenomenon is also supported by tracks 3 and 4. Track 4 was designed to follow the fluxgate, which separates the continental shelf from the deep ocean, and track 3 is further south parallel to track 4. The sea ice in track 4 is thicker than that in track 3 with modal values of 0.45 m for track 4 and 0.35 m for track 3. The ice of track 4 is relatively thinner in the middle section of the fluxgate than that in the west and east sections of the fluxgate.

In addition, the lowest 2% elevation method is applied to the IceBridge airborne data previously used with ICESat satellite data to derive total freeboard. It is found that the lowest elevation method could overestimate the freeboard. When comparing the ICESat freeboard with the 2013 OIB freeboard (2013 a) by using the same method, large interannual variability is observed, with no clear increase or decrease from the 2003–2008 ICESat era to 2013. This comparison, however, is limited by the fact that the locations and time periods of the tracks are not exactly the same.

Spatial distributions of freeboard, ICESat 2003–2008 and 2013 OIB with different methods, have a similar pattern, thinner in the center part (gray circle), and thicker in the east, north or more near coasts (but away from the polynyas). Though different methods have differences in absolute values, they are still able to reflect the same spatial distribution pattern, which suggests that the mean sea-ice thickness values are less affected by different methods and datasets. Comparison of mean sea-ice thickness
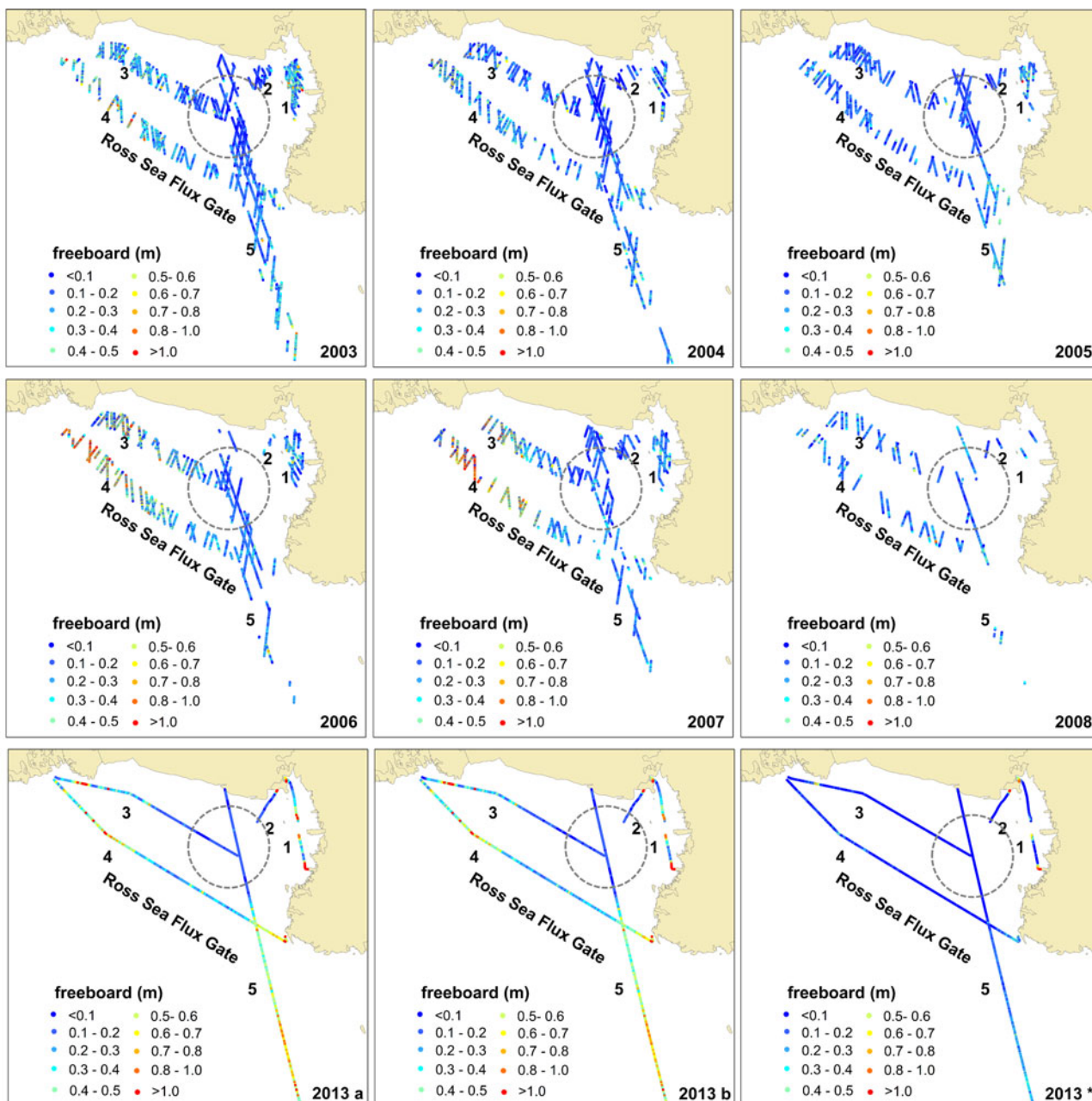
Fig. 12. Spatial distribution of total freeboard for each track from ICESat (2003–2008) and ATM (2013 a, 2013 b and 2013 *). Letters 'a', 'b' and symbol '*' following 2013 refer to the different methods used as in Figure 7. The gray circle represents the area with the lowest freeboard (the thinnest ice).

Table 1. Comparison of mean sea-ice thickness values along the fluxgate and estimation of exported ice volume based on area export data from Kwok and others (2017)

Thickness data sources	Mean sea-ice thickness (m)	Net ice area export (10^3 km² a⁻¹)	estimation of exported ice volume (km³ a⁻¹)
1995 Measurements	0.65 ± 0.33	~531	~345
2003 ICESat	0.87 ± 0.18	~884	~769
2004 ICESat	0.85 ± 0.17	~1263	~1074
2005 ICESat	0.67 ± 0.11	~1149	~770
2006 ICESat	1.19 ± 0.31	~739	~879
2007 ICESat	1.24 ± 0.33	~783	~971
2008 ICESat	0.77 ± 0.14	~979	~754
2013a ATM	0.60 ± 0.10	~827	~496
2013b ATM	0.55 ± 0.09	~827	~455
2013* ATM	0.48 ± 0.10	~827	~397

The 1995 measurements are shipboard data inside the fluxgate in the western Ross Sea during May–June 1995 (Jeffries and Adolphs, 1997). Letters 'a', 'b' and symbol '*' refer to the different methods used as in Figure 7.

values along the fluxgate, such as the one presented in this study could help provide a more accurate estimate of the ice volume over the continental shelf and thus better estimate SIP in the Ross Sea. Further examination and verification are forthcoming using ICESat-2 data as well as 2016 and 2017 airborne flights using the IcePod system (ATM and DMS) on NSF's C-130 aircraft.

References

Andersen O, Knudsen P and Stenseng L (2015) The DTU13 MSS (mean sea surface) and MDT (mean dynamic topography) from 20 years of satellite altimetry. IGFS *2014* **144**, 111–121. doi: 10.1007/1345_2015_182.

Andersen OB, Stenseng L, Piccioni G and Knudsen P (2016) The DTU15 MSS (Mean Sea Surface) and DTU15LAT (Lowest Astronomical Tide) reference surface. *ESA Living Planet Symposium 2016*.

Comiso JC, Kwok R, Martin S and Gordon AL (2011) Variability and trends in sea ice extent and ice production in the Ross Sea. *Journal of Geophysical Research: Oceans* **116**(C4). doi: 10.1029/2010JC006391.

Dieckmann GS and Hellmer HH (2010) The importance of sea ice: an overview. *Sea Ice* **2**, 1–22.

Dominguez R (2010) IceBridge DMS L1B geolocated and orthorectified images (IODMS1B, 2013). NASA Distributed Active Archive Center, National Snow and Ice Data Center, Boulder, CO. Digital media. Available at http://nsidc.org/data/iodms1b.html.

Drucker R, Martin S and Kwok R (2011) Sea ice production and export from coastal polynyas in the Weddell and Ross Seas. *Geophysical Research Letters* **38**(17). doi: 10.1029/2011GL048668.

Duong T (2007) Ks: Kernel density estimation and kernel discriminant analysis for multivariate data in R. *Journal of Statistical Software* **21**(7), 1–16. doi: http://hdl.handle.net/10.18637/jss.v021.i07.

Farrell SL, Laxon SW, McAdoo DC, Yi D and Zwally H (2009) Five years of Arctic sea ice freeboard measurements from the Ice, Cloud and land Elevation Satellite. *Journal of Geophysical Research: Oceans* **114**(C4). doi: 10.1029/2008JC005074.

Geiger C, Müller H-R, Samluk JP, Bernstein ER and Richter-Menge J (2015) Impact of spatial aliasing on sea-ice thickness measurements. *Annals of Glaciology* **56**(69), 353–362. doi: 10.3189/2015AoG69A644.

Gordon AL and Comiso JC (1988) Polynyas in the southern ocean. *Scientific American* **258**(6), 90–97.

Holland MM, Bitz CM and Weaver A (2001) The influence of sea ice physics on simulations of climate change. *Journal of Geophysical Research: Oceans* **106**(C9), 19639–19655. doi: 10.1029/2000JC000651.

Jacobs SS and Giulivi CF (2010) Large multidecadal salinity trends near the Pacific–Antarctic continental margin. *Journal of Climate* **23**(17), 4508–4524. doi: 10.1175/2010JCLI3284.1.

Jeffries MO and Adolphs U (1997) Early winter ice and snow thickness distribution, ice structure and development of the western Ross Sea pack ice between the ice edge and the Ross Ice Shelf. *Antarctic Science* **9**(2), 188–200. doi: 10.1017/S0954102097000242.

Jeffries MO, Li S, Jana RA, Krouse HR and Hurst-Cushing B (1998) Late winter first-year ice floe thickness variability, seawater flooding and snow ice formation in the Amundsen and Ross Seas. In Jeffries O (ed.) *Antarctic Sea Ice: Physical Processes, Interactions and Variability, Antarct. Res. Ser., vol. 74*. Washington DC: AGU, pp. 69–87.

Kern S, Ozsoy-Çiçek B and Worby A (2016) Antarctic sea-ice thickness retrieval from ICESat: inter-comparison of different approaches. *Remote Sensing* **8**(7), 538. doi: 10.3390/rs8070538.

Kern S and Spreen G (2015) Uncertainties in Antarctic sea-ice thickness retrieval from ICESat. *Annals of Glaciology* **56**(69), 107–119. doi: 10.3189/2015AoG69A736.

Krabill W (2013) IceBridge ATM L1B elevation and return strength, Version 2. *Boulder, Colorado USA: NASA DAAC at the National Snow and Ice Data Center*.

Kurtz NT and 6 others (2009) Estimation of sea ice thickness distributions through the combination of snow depth and satellite laser altimetry data. *Journal of Geophysical Research: Oceans* **114**(C10). doi: 10.1029/2009JC005292.

Kurtz N and 8 others (2013) Sea ice thickness, freeboard, and snow depth products from Operation IceBridge airborne data.

Kurtz N and Markus T (2012) Satellite observations of Antarctic sea ice thickness and volume. *Journal of Geophysical Research: Oceans* **117**(C8). doi: 10.1029/2012JC008141.

Kusahara K, Reid P, Williams GD, Massom R and Hasumi H (2018) An ocean-sea ice model study of the unprecedented Antarctic sea ice minimum in 2016. *Environmental Research Letters* **13**(8), 084020. doi: 10.1088/1748-9326/aad624.

Kwok R (2005) Ross Sea ice motion, area flux, and deformation. *Journal of Climate* **18**(18), 3759–3776. doi: 10.1175/JCLI3507.1.

Kwok R, Cunningham GF, Manizade S and Krabill W (2012) Arctic Sea ice freeboard from IceBridge acquisitions in 2009: estimates and comparisons with ICESat. *Journal of Geophysical Research: Oceans* **117**(C2). doi: 10.1029/2011JC007654.

Kwok Ron and Kacimi Sahra (2018) Three years of sea ice freeboard, snow depth, and ice thickness of the Weddell Sea from Operation IceBridge

and CryoSat-2. *The Cryosphere*, **12**(8), 2789–2801. doi: http://dx.doi.org/10.5194/tc-12-2789-2018.

Kwok R, Pang SS and Kacimi S (2017) Sea ice drift in the Southern Ocean: regional patterns, variability, and trends. *Elementa: Science of the Anthropocene* **5**, 32. doi: 10.1525/elementa.226.

Kwok R and Rothrock DA (2009) Decline in Arctic sea ice thickness from submarine and ICESat records: 1958-2008. *Geophysical Research Letters* **36**(15). doi: 10.1029/2009GL039035.

Kwok R, Zwally HJ and Yi D (2004) ICESat observations of Arctic sea ice: a first look. *Geophysical Research Letters* **31**(16). doi: 10.1029/2004GL020309.

Li H and 6 others (2018) Spatio-temporal variability of Antarctic sea-ice thickness and volume obtained from ICESat data using an innovative algorithm. *Remote Sensing of Environment* **219**, 44–61. doi: 10.1016/j.rse.2018.09.031

Li J and Heap AD (2008) A review of spatial interpolation methods for environmental scientists.

Markus T and 24 others (2017) The Ice, Cloud, and land Elevation Satellite-2 (ICESat-2): science requirements, concept, and implementation. *Remote Sensing of Environment* **190**, 260–273. doi: 10.1016/j.rse.2016.12.029.

Markus T and Cavalieri DJ (1998) Snow Depth Distribution Over Sea Ice in the Southern Ocean From Satellite Passive Microwave Data. *Antarctic Sea Ice: Physical Processes, Interactions and Variability* **74**, 19–39. doi: 10.1029/AR074p0019.

Martin S, Drucker RS and Kwok R (2007) The areas and ice production of the western and central Ross Sea polynyas, 1992–2002, and their relation to the B-15 and C-19 iceberg events of 2000 and 2002. *Journal of Marine Systems* **68**(1–2), 201–214. doi: 10.1016/j.jmarsys.2006.11.008.

Meier WN (2017) Losing Arctic sea ice: observations of the recent decline and the long-term context. *Sea Ice*, 290–303.

Nababan B, Hakim MR and Panjaitan JP (2018) Waveform identification and retracking analyses of Jason-2 altimeter satellite data for improving sea surface height estimation in Southern Java Island Waters and Java Sea, Indonesia. *IOP Conference Series: Earth and Environmental Science*, IOP Publishing, 012057. (1). doi: 10.1088/1755-1315/149/1/012057.

Onana V-D-P and 5 others (2013) A sea-ice lead detection algorithm for use with high-resolution airborne visible imagery. *IEEE Transactions on Geoscience and Remote Sensing* **51**, 38–56. doi: 10.1109/TGRS.2012.2202666.

Ozsoy-Cicek B, Ackley S, Xie H, Yi D and Zwally J (2013) Sea ice thickness retrieval algorithms based on in situ surface elevation and thickness values for application to altimetry. *Journal of Geophysical Research: Oceans* **118**(8), 3807–3822. doi: 10.1002/jgrc.20252, 2013.

Parish TR (1988) Surface winds over the Antarctic continent: a review. *Reviews of Geophysics* **26**(1), 169–180. doi: 10.1029/RG026i001p00169.

Parkinson CL (2019) A 40-y record reveals gradual Antarctic sea ice increases followed by decreases at rates far exceeding the rates seen in the Arctic. *Proceedings of the National Academy of Sciences* **116**(29), 14414–14423. doi: 10.1073/pnas.1906556116.

Parkinson CL and Cavalieri DJ (2012) Antarctic sea ice variability and trends, 1979-2010. *The Cryosphere* **6**(4), 871. doi: 10.5194/tc-6-871-2012.

Rinke A, Maslowski W, Dethloff K and Clement J (2006) Influence of sea ice on the atmosphere: a study with an Arctic atmospheric regional climate model. *Journal of Geophysical Research: Atmospheres* **111**(D16). doi: 10.1029/2005JD006957.

Screen JA and Simmonds I (2010) The central role of diminishing sea ice in recent Arctic temperature amplification. *Nature* **464**(7293), 1334. doi: 10.1038/nature09051.

Simmonds I (2015) Comparing and contrasting the behaviour of Arctic and Antarctic sea ice over the 35 year period 1979-2013. *Annals of Glaciology* **56**(69), 18–28. doi: 10.3189/2015AoG69A909.

Skourup H and 8 others (2017) An assessment of state-of-the-art mean sea surface and geoid models of the Arctic Ocean: implications for sea ice freeboard retrieval. *Journal of Geophysical Research: Oceans* **122**(11), 8593–8613. doi: 10.1002/2017JC013176.

Stammerjohn S, Massom R, Rind D and Martinson D (2012) Regions of rapid sea ice change: an inter-hemispheric seasonal comparison. *Geophysical Research Letters* **39**(6). doi: 10.1029/2012GL050874.

Studinger M (2016) IceBridge ATM L2 Icessn Elevation, Slope, and Roughness, Version 2. Updated.

Stuecker MF, Bitz CM and Armour KC (2017) Conditions leading to the unprecedented low Antarctic sea ice extent during the 2016 austral spring season. *Geophysical Research Letters* **44**(17), 9008–9019. doi: 10.1002/2017GL074691.

Turner J and 6 others (2017) Unprecedented springtime retreat of Antarctic sea ice in 2016. *Geophysical Research Letters* **44**(13), 6868–6875. doi: 10.1002/2017GL073656.

Turner J and Overland J (2009) Contrasting climate change in the two polar regions. *Polar Research* **28**(2), 146–164. doi: 10.1111/j.1751-8369.2009.00128.x.

Wang X, Guan F, Liu J, Xie H and Ackley S (2016) An improved approach of total freeboard retrieval with IceBridge Airborne Topographic Mapper (ATM) elevation and Digital Mapping System (DMS) images. *Remote Sensing of Environment* **184**, 582–594. doi: 10.1016/j.rse.2016.08.002.

Wang X, Xie H, Ke Y, Ackley SF and Liu L (2013) A method to automatically determine sea level for referencing snow freeboards and computing sea ice thicknesses from NASA IceBridge airborne LIDAR. *Remote Sensing of Environment* **131**, 160–172. doi: 10.1016/j.rse.2012.12.022.

Weissling B, Lewis M and Ackley S (2011) Sea-ice thickness and mass at ice station Belgica, Bellingshausen Sea, Antarctica. *Deep Sea Research Part II: Topical Studies in Oceanography* **58**(9), 1112–1124. doi: 10.1016/j.dsr2.2010.10.032.

Xia W and Xie H (2018) Assessing three waveform retrackers on sea ice freeboard retrieval from Cryosat-2 using Operation IceBridge Airborne altimetry datasets. *Remote Sensing of Environment* **204**, 456–471. doi: 10.1016/j.rse.2017.10.010.

Xie H and 7 others (2011) Sea-ice thickness distribution of the Bellingshausen Sea from surface measurements and ICESat altimetry. *Deep Sea Research Part II: Topical Studies in Oceanography* **58**(9), 1039–1051. doi: 10.1016/j.dsr2.2010.10.038.

Xie H, Tekeli AE, Ackley SF, Yi D and Zwally HJ (2013) Sea ice thickness estimations from ICESat Altimetry over the Bellingshausen and Amundsen Seas, 2003–2009. *Journal of Geophysical Research: Oceans* **118**(5), 2438–2453. doi: 10.1002/jgrc.20179.

Zhang J (2007) Increasing Antarctic sea ice under warming atmospheric and oceanic conditions. *Journal of Climate* **20**(11), 2515–2529. doi: 10.1175/JCLI4136.1.

Zwally H and 9 others (2002) ICESat's laser measurements of polar ice, atmosphere, ocean, and land. *Journal of Geodynamics* **34**(3–4), 405–445. doi: 10.1016/S0264-3707(02)00042-X.

Zwally HJ, Yi D, Kwok R and Zhao Y (2008) ICESat measurements of sea ice freeboard and estimates of sea ice thickness in the Weddell Sea. *Journal of Geophysical Research: Oceans* **113**(C2). doi: 10.1029/2007JC004284.